Discrimination of granulocyte subtypes from light scattering: theoretical analysis using a granulated sphere model

Yurkin, M.A.; Semyanov, K.A.; Maltsev, V.P.; Hoekstra, A.G.

Link to publication

Discrimination of granulocyte subtypes from light scattering: theoretical analysis using a granulated sphere model

Maxim A. Yurkin[1,2,*], Konstantin A. Semyanov[2], Valeri P. Maltsev[2,3,4], and Alfons G. Hoekstra[1]

[1]*Faculty of Science, University of Amsterdam, Kruislaan 403, 1098 SJ, Amsterdam, The Netherlands*
[2]*Institute of Chemical Kinetics and Combustion, Siberian Branch of the Russian Academy of Sciences, Institutskaya 3, 630090, Novosibirsk, Russia*
[3]*Novosibirsk State University, Pirogova 2, 630090, Novosibirsk, Russia*
[4]*State Research Center of Virology and Biotechnology "VECTOR", Koltsovo, 630559, Novosibirsk Region, Russia*
*[*myurkin@science.uva.nl](mailto:myurkin@science.uva.nl)*

Abstract: We perform extensive simulations of light scattering by a granulated sphere in the size and refractive index range of human granulated leucocytes using the discrete dipole approximation. We calculate total and depolarized side scattering signals as a function of the size and refractive indices of cell and granules, and the granule volume fraction. Using typical parameters derived from the literature data on granulocyte morphology, we show that differences between experimentally measured signals of two granulocyte subtypes can be explained solely by the difference in their granule sizes. Moreover, the calculated depolarization ratio quantitatively agrees with experimental results. We also use the Rayleigh-Debye-Gans approximation and its second order extension to derive analytical expressions for side scattering signals. These expressions qualitatively describe the scaling of signals with varying model parameters obtained by rigorous simulations, and even lead to quantitative agreement in some cases. Finally, we show and discuss the dependence of extinction efficiency and asymmetry parameter on size and volume fraction of granules.

References and links

1. M. I. Mishchenko, L. D. Travis, and A. A. Lacis, *Scattering, Absorption, and Emission of Light by Small Particles*, (Cambridge University Press, Cambridge, 2002).
2. P. Chylek, G. Videen, D. J. W. Geldart, J. S. Dobbie, and H. C. W. Tso, "Effective medium approximations for heterogeneous particles," in *Light Scattering by Nonspherical Particles, Theory, Measurements, and Applications,* M. I. Mishchenko, J. W. Hovenier, and L. D. Travis, eds. (Academic Press, New York, 2000), pp. 273-308.
3. L. Kolokolova and B. A. S. Gustafson, "Scattering by inhomogeneous particles: microwave analog experiments and comparison to effective medium theories," J. Quantum Spectrosc. Radiat. Transfer **70**, 611-625 (2001).
4. N. V. Voshchinnikov, V. B. Il'in, and T. Henning, "Modelling the optical properties of composite and porous interstellar grains," Astron. Astrophys. **429**, 371-381 (2005).
5. M. I. Mishchenko, L. D. Travis, and A. A. Lacis, *Multiple Scattering of Light by Particles: Radiative Transfer and Coherent Backscattering*, (Cambridge University Press, Cambridge, 2006).
6. Y. L. Xu and B. A. S. Gustafson, "Comparison between multisphere light-scattering calculations: Rigorous solution and discrete-dipole approximation," Astrophys. J. **513**, 894-909 (1999).
7. D. W. Mackowski and M. I. Mishchenko, "Calculation of the T matrix and the scattering matrix for ensembles of spheres," J. Opt. Soc. Am. A **13**, 2266-2278 (1996).
8. M. I. Mishchenko, L. Liu, D. W. Mackowski, B. Cairns, and G. Videen, "Multiple scattering by random particulate media: exact 3D results," Opt. Express **15**, 2822-2836 (2007).
9. A. Taflove and S. C. Hagness, *Advances in Computational Electrodynamics: the Finite-Difference Time-Domain Method*, 3rd ed., (Artech House, Boston, 2005).

10. M. A. Yurkin and A. G. Hoekstra, "The discrete dipole approximation: an overview and recent developments," J. Quantum. Spectrosc. Radiat. Transfer **106**, 558-589 (2007).
11. K. Lumme and J. Rahola, "Light-scattering by porous dust particles in the discrete-dipole approximation," Astrophys. J. **425**, 653-667 (1994).
12. A. K. Dunn, "Modelling of light scattering from inhomogeneous biological cells," in *Optics of Biological Particles,* A. G. Hoekstra, V. P. Maltsev, and G. Videen, eds. (Springer, London, 2006), pp. 19-29.
13. *Flow Cytometry and Sorting*, 2nd ed., M. R. Melamed, T. Lindmo, and M. L. Mendelson, eds. (Wiley-Liss, New York, 1990).
14. B. G. de Grooth, L. W. Terstappen, G. J. Puppels, and J. Greve, "Light-scattering polarization measurements as a new parameter in flow cytometry," Cytometry **8**, 539-544 (1987).
15. S. Suzuki and N. Eguchi, "Leukocyte differential analysis in multiple laboratory species by a laser multi-angle polarized light scattering separation method," Exp. Anim. **48**, 107-114 (1999).
16. M. Hedhammar, M. Stenvall, R. Lonneborg, O. Nord, O. Sjolin, H. Brismar, M. Uhlen, J. Ottosson, and S. Hober, "A novel flow cytometry-based method for analysis of expression levels in Escherichia coli, giving information about precipitated and soluble protein," J. Biotech. **119**, 133-146 (2005).
17. F. Lavergne-Mazeau, A. Maftah, Y. Cenatiempo, and R. Julien, "Linear correlation between bacterial overexpression of recombinant peptides and cell light scatter," Appl. Environ. Microbiol. **62**, 3042-3046 (1996).
18. L. W. M. M. Terstappen, B. G. de Grooth, K. Visscher, F. A. van Kouterik, and J. Greve, "Four-parameter white blood cell differential counting based on light scattering measurements," Cytometry **9**, 39-43 (1988).
19. S. Lavigne, M. Bosse, L. P. Boulet, and M. Laviolette, "Identification and analysis of eosinophils by flow cytometry using the depolarized side scatter-saponin method," Cytometry **29**, 197-203 (1997).
20. S. L. Perkins, "Normal blood and bone marrow values in humans," in *Wintrobe's Clinical Hematology,* 11th ed., J. P. Greer, J. Foerster, and J. N. Lukens, eds., (Lippincott Williams & Wilkins Publishers, Baltimore, USA, 2003), pp. 2738-2741.
21. K. M. Skubitz, "Neutrophilic leukocytes," in *Wintrobe's Clinical Hematology,* 11th ed., J. P. Greer, J. Foerster, and J. N. Lukens, eds. (Lippincott Williams & Wilkins Publishers, Baltimore, USA, 2003), pp. 267-310.
22. P. Lacy, A. B. Becker, and R. Moqbel, "The human eosinophil," in *Wintrobe's Clinical Hematology,* 11th ed., J. P. Greer, J. Foerster, and J. N. Lukens, eds., (Lippincott Williams & Wilkins Publishers, Baltimore, USA, 2003), pp. 311-334.
23. H. P. Ting-Beall, D. Needham, and R. M. Hochmuth, "Volume and osmotic properties of human neutrophils," Blood **81**, 2774-2780 (1993).
24. P. Brederoo, J. van der Meulen, and A. M. Mommaas-Kienhuis, "Development of the granule population in neutrophil granulocytes from human bone marrow," Cell Tissue Res. **234**, 469-496 (1983).
25. L. W. Diggs, D. Sturm, and A. Bell, *The Morphology of Human Blood Cells*, 5th ed., (Abbott Laboratories, Abbott Park, IL 60064, 1985).
26. G. J. Puppels, H. S. P. Garritsen, G. M. J. Segers-Nolten, F. F. M. de Mul, and J. Greve, "Raman microspectroscopic approach to the study of human granulocytes," Biophys. J. **60**, 1046-1056 (1991).
27. S. A. Livesey, E. S. Buescher, G. L. Krannig, D. S. Harrison, J. G. Linner, and R. Chiovetti, "Human neutrophil granule heterogeneity: immunolocalization studies using cryofixed, dried and embedded specimens," Scanning Microsc. Suppl **3**, 231-239 (1989).
28. W. T. Daems, "On the fine structure of human neutrophilic leukocyte granules," J. Ultrastruct. Res. **24**, 343-348 (1968).
29. O. W. Bjerrum, "Human neutrophil structure and function with special reference to cytochrome b559 and beta 2-microglobulin," Dan. Med. Bull. **40**, 163-189 (1993).
30. D. F. Bainton, "Neutrophilic leukocyte granules: from structure to function," Adv. Exp. Med. Biol. **336**, 17-33 (1993).
31. A. E. Zharinov, P. A. Tarasov, A. N. Shvalov, K. A. Semyanov, D. R. van Bockstaele, and V. P. Maltsev, "A study of light scattering of mononuclear blood cells with scanning flow cytometry," J. Quantum. Spectrosc. Radiat. Transfer **102**, 121-128 (2006).
32. K. A. Semyanov, A. E. Zharinov, P. A. Tarasov, M. A. Yurkin, I. G. Skribunov, D. R. van Bockstaele, and V. P. Maltsev, "Optics of leucocytes," in *Optics of Biological Particles,* A. G. Hoekstra, V. P. Maltsev, and G. Videen, eds. (Springer, London, 2006), pp. 253-264.
33. C. F. Bohren and D. R. Huffman, *Absorption and scattering of Light by Small Particles*, (Wiley, New York, 1983).
34. M. A. Yurkin, V. P. Maltsev, and A. G. Hoekstra, "The discrete dipole approximation for simulation of light scattering by particles much larger than the wavelength," J. Quant. Spectrosc. Radiat. Transfer **106**, 546-557 (2007).
35. "Amsterdam DDA," http://www.science.uva.nl/research/scs/Software/adda (2007).
36. "Description of the national compute cluster Lisa," http://www.sara.nl/userinfo/lisa/description/ (2005).
37. N. W. Ashcroft and J. Lekner, "Structure and resistivity of liquid metals," Phys. Rev. **145**, 83-90 (1966).
38. M. P. Allen and D. J. Tildesley, *Computer Simulations of Liquids*, (Oxford University Press, Oxford, 1989).
39. V. V. Tuchin, L. V. Wang, and D. A. Zimnyakov, *Optical Polarization in Biomedical Applications*, (Springer, Berlin, 2006).

1. Introduction

Simulation of light scattering by homogeneous particles with simple shapes, such as spheroids, is relatively easy [1]. Unfortunately, most natural particles are inhomogeneous and have a complex shape. A broad class of such particles can be characterized by a matrix with multiple inclusions (granules). A number of approximations exist to simulate light scattering by these particles which fall in one of two connected realms: effective medium theories (EMTs) [2-4] or radiative transfer theories [5]. The latter is especially relevant when an infinite medium is considered or granule positions randomly fluctuate with significant amplitude during the observation time.

However, in many cases none of these approximations is accurate enough and rigorous light scattering theories are required. The superposition T-matrix method allows simulation of light scattering by clusters of spheres [6,7], which is a particular case of a granulated particle when the matrix is vacuum. Recently Mishchenko *et al.* [8] studied clusters of spheres with respect to radiative transfer theories. Apart from that, only general methods like the finite difference time domain method (FDTD) [9] or the discrete dipole approximation (DDA) [10] are capable of simulating light scattering by arbitrarily shaped granulated particles. Most researchers who studied granulated particles are concerned with astrophysical or atmospheric applications [3,4,8,11], while our main application – light scattering by biological cells – is a much less studied field.

Biological cells, when suspended in liquid, have an important advantage with respect to the light scattering simulation. Their relative refractive index is close to unity. This accelerates the rigorous methods and improves the accuracy of the EMTs and other approximate theories. FDTD simulation of light scattering by biological cells was performed in a number of manuscripts by Dunn and coworkers (summarized in [12]). To the best of our knowledge, these are the only studies that include cell organelles and granules in rigorous light scattering modeling. The main conclusion is that side scattering by biological cells are mainly determined by small granules, which agrees with the general notion of flow cytometry [13]. However, only the dependence on the volume fraction and not on the size of the granules was studied.

Study of light scattering by granulated biological cells is motivated by several empirical techniques that use the dependence of light scattering signals measured by flow cytometer on the characteristics of the granules [14-17]. All these techniques are successfully used in practice but lack a rigorous theoretical foundation. For instance, production of the inclusion bodies consisting of protein synthesized by *E. coli* cells was found to correlate with forward scattering [16,17], which can be qualitatively explained by the increase of total amount of matter that scatters light inside the cells. Probably, the most fascinating application of light scattering to characterize granulated cells are the results of de Grooth, Terstappen and coworkers [14,18,19], who showed that neutrophils and eosinophils can be discriminated by their depolarized side scattering intensity $I_\perp$. This result was extended to other species by Suzuki and Eguchi [15]. The values for light scattering signals are given in arbitrary units by de Grooth *et al.* [14] and, hence, can be compared to other studies only qualitatively. However, the ratios of the signals, which are also provided, can be compared quantitatively to predictions of any models, thus providing a stringent test of the latter.

Granulocytes are the most numerous type of leukocytes, consisting of three subtypes: neutrophils, eosinophils, and basophils. Their abundance relative to all leukocytes in normal condition is in the ranges 46–73%, 0–4.4%, and 0.2–1.2% respectively [20]. The major role of neutrophils is to protect the host against infectious agents. To accomplish this task, the neutrophil must first sense infection, migrate to the site of the infecting organism, and then destroy the infectious agents [21]. Although rare in healthy individuals, the eosinophil is prominent in peripheral blood and tissue in association with various disease conditions including allergy, inflammatory responses against metazoan helminthic parasites, and certain skin and malignant conditions [22].
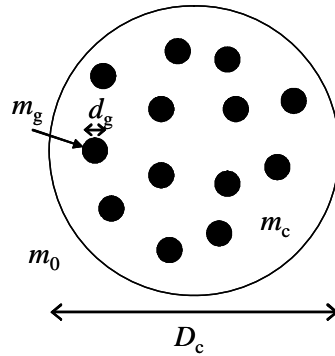
Fig. 1. The granulated sphere model. All granules are identical and randomly positioned.

In this manuscript we aim at two goals: to get general insight into light scattering by index-matching granulated particles much larger than the wavelength and to rigorously explain why eosinophils and neutrophils have different $I_\perp$. For that we construct a simple model of granulocytes in Section 2, starting from literature data on its morphology. In Section 3 we specify the total and depolarized side scattering signals measured by flow cytometers. We derive analytical expressions for these signals using the Rayleigh-Debye-Gans (RDG) approximation and its second-order extension in Sections 4 and 5 respectively. We show the results of extensive DDA simulations in Section 6, comparing them with predictions of approximate theories and known experimental results. We conclude the manuscript in Section 7 and discuss perspectives for characterizing granulated particles, specifically granulocytes, with light scattering.

2. Simple granulocyte model and DDA simulations

Both neutrophils and eosinophils have a size of 10–15 μm as measured in blood smears [21]. However Ting-Beall *et al.* [23] reported that a normal suspended neutrophil has a volume of $299 \pm 64\ \mu m^3$, which corresponds to a diameter $8.3 \pm 0.6\ \mu m$ (intervals correspond to two standard deviations). A similar value for the diameter of mature neutrophils ($8.3 \pm 1.2\ \mu m$) was obtained by Brederoo *et al.* [24] using electron microscopy. For eosinophils a value of 8 μm has been reported [22]. The nucleus is separated into definite lobes with a very narrow filament or strand connecting the lobes. Usually, two or three lobes are observed [22,25,26].

Neutrophils contain two major types of granules: azurophilic and specific granules, although more minor classes can be specified [24,27,28]. Azurophilic granules are larger and more dense than the specific ones, and the ratio of their numbers is 1/2–1/3 [29]. A typical size of azurophilic granules is 500 nm, whereas specific granules are either spherical with a size of 200 nm (Livesey, *et al.,* [27] reported the range 100–250 nm) or rod shaped (130×1000 nm) [30]. On average a cell cross section contains 200–300 granules [30], the total number per whole cell is 1900–6300, with a total volume of 30 μm^3 [29]. Eosinophils contain three major classes of granules: crystalloid, primary, and small granules. Crystalloid granules measure 0.5–0.8 μm in diameter [22] (Puppels *et al.* [26] reported another range: 0.9–1.3 μm) and contain crystalline electron-dense cores surrounded by an electron-lucent matrix. There are approximately 200 crystalloid granules in each cell [22,26]. Primary granules measure 0.1–0.5 μm in diameter and are less abundant than crystalloid granules. Small granules are even smaller than primary ones [22].

We use a granulated sphere as a model for granulocytes (see Fig. 1). The sphere contains no nucleus and all the granules are identical and randomly placed inside the cell. Thus, we compromise between realistic shapes (cf. [12]) and a general fundamental approach (cf. [8]). We are able to study the dependence of light scattering of each of the particle parameters independently, and at the same time to quantitatively describe at least the depolarization ratios of neutrophils and eosinophils (see Section 6).

In the following we describe the default parameters of the model. The diameter of the cell $D_c = 8\,\mu m$ and volume fraction of granules $f = 0.1$ correspond to the above data on morphology of both neutrophils and eosinophils. Dunn collected information on refractive indices of the cell cytoplasm and constituents from several sources [12]. However, the ranges are broad, which makes it hard to select a particular value. We set the cytoplasm refractive indices, relative to the medium (for which we consider buffered saline $m_0 = 1.337$), to $m_c = 1.015$, which corresponds to the values obtained by fitting experimental light scattering patterns of lymphocytes by a multi-layered sphere model [31,32]. For the granules we set the relative refractive index to the upper limit as if granules consist entirely of proteins, $m_g = 1.2$. This choice exaggerates all light scattering effects of granules; however, as we will show, all conclusions also are valid for smaller m_g. We completely neglect absorption in this study, and set the wavelength to that of a $0.66\,\mu m$ semiconductor laser, which is $0.4936\,\mu m$ in the medium. The main variable is the granule diameter d_g, which is varied from 0.075 to $2\,\mu m$. The lower limit is determined by the size of the dipole in DDA, which was set to $0.041\,\mu m$ for all simulations, corresponding to 12 dipoles per wavelength in the outer medium. Each DDA simulation depends on random granule placement, therefore we repeat it 10 times and show mean value $\pm\, 2\times SD$ (standard deviation) for each simulated value. In addition, we simulated the result for effectively $d_g = 0$, by using the Mie theory applied to a homogenous sphere, where the refractive index is obtained by Maxwell-Garnett EMT [33]. Since all refractive indices are close to unity, the differences between most EMTs are negligible.

We also varied some of the parameters from their default values. To limit the number of DDA simulations and keep the time of this study feasible we varied each parameter with others fixed. For each set of parameters a whole range of d_g was calculated. We tried four additional values of f: 0.02, 0.05, 0.2, and 0.3, two values of D_c: 4 and $14\,\mu m$, two of m_g: 1.1 and 1.15, and one of $m_c = 1$, i.e. no cytoplasm at all (actually we used $m_c = 1.000001$ because of the limitations of the current code).

As a numerical implementation of the DDA we have used the ADDA computer code v.0.76, which is capable of running on a cluster of computers (parallelizing a single DDA computation), allowing simulating light scattering by scatterers much larger than a wavelength [34,35]. In this manuscript we use the default ADDA settings for dipole polarizability (lattice dispersion relation), iterative method (quasi minimal residual method), and convergence threshold (relative residual norm less than 10^{-5}) and employ the built-in granule generator. For each particle we calculated Q_{ext}, $<\cos\theta>$, and the whole Mueller matrix for the whole scattering angle with steps of $0.5°$ and $5°$ in polar θ and azimuthal φ angles respectively. Moreover, we refined the grid to $0.5°$ step in φ near the side scattering direction to accurately compute the signals described in Section 3. All simulations were run on the Dutch compute cluster LISA [36]. Typical simulation time is half an hour on 8 nodes (each node has dual Intel Xeon 3.4 GHz processor with 4 GB RAM), but it is about 1.5 hours on 16 nodes for $D_c = 14\,\mu m$.

3. Orthogonal light scattering

We simulate the side scattering signals exactly as described by de Grooth *et al.* [14]. The incident light propagates along the *z*-axis and is polarized along the *x*-axis, and the particle is located in the origin. The exact side scattering direction is along the *y*-axis. A lens focused on the particles projects the scattered light on the photodetector; both the lens and the photodetector are centered around and orthogonal to the *y*-axis. A rectangular diaphragm placed before the lens limits the collection scattering angles to $\theta = 90° \pm \Delta\theta$ and $\varphi = 90° \pm \Delta\varphi$. The default values are $\Delta\theta = \Delta\varphi = 25°$. The measured signals are the total side scattering intensity collected by the photodetector I_{SS} and the total depolarized intensity $I_\perp$, when a polarizer with polarization axis along the *z*-axis is placed before the photodetector. The depolarization ratio is defined as $D_{SS} = I_\perp / I_{SS}$.

In the original paper [14] an expression of I_{SS} and $I_{\perp}$ in terms of the amplitude scattering matrix (S_i) is derived, however it has a typographical error in one sign. Therefore, we present the corrected derivation in the following and also derive an expression in terms of the Mueller scattering matrix (S_{ij}). We denote the radius vector of a point on the lens as $\mathbf{r}$, and scattering direction $\mathbf{n} = \mathbf{r}/r$, which corresponds to scattering angles θ and φ. We introduce unity vectors $\mathbf{e}_{\perp}$ and $\mathbf{e}_{\parallel}$ orthogonal and parallel to the scattering plane respectively, which are the local basis for scattered wave in point $\mathbf{r}$, i.e. $\{\mathbf{e}_{\perp}, \mathbf{e}_{\parallel}, \mathbf{n}\}$ is a right-handed orthogonal basis (according to Bohren and Huffman [33]). These vectors are connected to the basis vectors of a spherical coordinate system by $\mathbf{e}_{\parallel} = \mathbf{e}_{\theta}$, $\mathbf{e}_{\perp} = -\mathbf{e}_{\varphi}$. We assume that incident light has unity amplitude. Then two components of the scattered electric field in point $\mathbf{r}$ (before the lens) is given by:

$$E_{\perp}^{sca} = (S_4 \cos\varphi + S_1 \sin\varphi)\frac{e^{ikr}}{-ikr}, \; E_{\parallel}^{sca} = (S_2 \cos\varphi + S_3 \sin\varphi)\frac{e^{ikr}}{-ikr}. \tag{1}$$

The lens rotates the propagation vector of the scattered wave from $\mathbf{n}$ to $\mathbf{e}_y$ together with the electric field vector.

We introduce the following auxiliary unity vectors:

$$\mathbf{e}_1 = (\mathbf{e}_y \times \mathbf{n})/|\mathbf{e}_y \times \mathbf{n}|, \; \mathbf{e}_2 = \mathbf{n} \times \mathbf{e}_1, \tag{2}$$

which form two right-handed orthogonal bases: $\{\mathbf{e}_1, \mathbf{e}_2, \mathbf{n}\}$ and $\{\mathbf{e}_1, \mathbf{e}_3, \mathbf{e}_y\}$. The mapping of scattered electric field in basis $\{\mathbf{e}_{\perp}, \mathbf{e}_{\parallel}, \mathbf{n}\}$ into the electric field on the detector in basis $\{\mathbf{e}_z, \mathbf{e}_x, \mathbf{e}_y\}$ (components E_z^{det} and E_x^{det}) is performed in several steps

$$\{\mathbf{e}_{\perp}, \mathbf{e}_{\parallel}, \mathbf{n}\} \xrightarrow{R_{\eta_1}(\mathbf{n})} \{\mathbf{e}_1, \mathbf{e}_2, \mathbf{n}\} \xrightarrow{\text{lens}} \{\mathbf{e}_1, \mathbf{e}_3, \mathbf{e}_y\} \xrightarrow{R_{\eta_2}(\mathbf{e}_y)} \{\mathbf{e}_z, \mathbf{e}_x, \mathbf{e}_y\}, \tag{3}$$

where $R_{\eta}(\mathbf{e})$ denotes the rotation by angle η around the vector $\mathbf{e}$, which changes the components of the electric field accordingly. The lens transformation does not change the component of the electric field along $\mathbf{e}_1$ and directly maps the component along $\mathbf{e}_2$ to the component along $\mathbf{e}_3$. Therefore the components E_z^{det} and E_x^{det} can be obtained from $E_{\perp}^{sca}$ and $E_{\parallel}^{sca}$ by rotation of the reference frame by the angle $\eta = \eta_1 + \eta_2$:

$$E_z^{det} = E_{\perp}^{sca} \cos\eta + E_{\parallel}^{sca} \sin\eta, \; E_x^{det} = -E_{\perp}^{sca} \sin\eta + E_{\parallel}^{sca} \cos\eta. \tag{4}$$

It is easy to show from geometrical considerations that

$$\tan\eta_1 = e_{\perp y}/e_{\parallel y} = -\sec\theta \cot\varphi, \; \tan\eta_2 = n_z/n_x = \sec\varphi \cot\theta, \tag{5}$$

$$\cos\eta = \frac{\cos\theta\cos\varphi}{1+\sin\theta\sin\varphi}, \; \sin\eta = -\frac{\sin\theta+\sin\varphi}{1+\sin\theta\sin\varphi}. \tag{6}$$

The corresponding angle-resolved total and depolarized intensities, which are sensed by the detector, are

$$J_{SS} = \left|E_x^{det}\right|^2 + \left|E_z^{det}\right|^2, \; J_{\perp} = \left|E_z^{det}\right|^2. \tag{7}$$

Using Eqs. (1), (4), and (7) and the definition of the Mueller scattering matrix in terms of the amplitude scattering matrix [33] one can obtain:

$$J_{SS}(\theta,\varphi) = \frac{1}{k^2 r^2}\left[S_{11} + S_{12}\cos(2\varphi) + S_{13}\sin(2\varphi)\right], \tag{8}$$

$$J_{\perp}(\theta,\varphi) = \frac{1}{2k^2 r^2}\{S_{11} - S_{21}\cos(2\eta) + S_{31}\sin(2\eta)$$
$$+ \left[S_{12} - S_{22}\cos(2\eta) + S_{32}\sin(2\eta)\right]\cos(2\varphi) + \left[S_{13} - S_{23}\cos(2\eta) + S_{33}\sin(2\eta)\right]\sin(2\varphi)\}. \tag{9}$$

The same result can be obtained using the Mueller matrix formalism.

The final signals, measured by the detector, are proportional to the intensities integrated over the scattering aperture:

$$I_{SS,\perp} = \kappa \iint_{\text{apert.}} d\varphi\, d\theta\, r^2 \sin\theta\, J_{SS,\perp}(\theta,\varphi). \tag{10}$$

We choose the proportionality coefficient $\kappa = k^2/(4\Delta\theta\Delta\varphi)$, so that I_{SS} and $I_\perp$ are linear combinations of the Mueller matrix elements averaged over the scattering aperture. Moreover, in the limit of infinitesimal small aperture, the expressions are especially simple:

$$\Delta\theta, \Delta\varphi \to 0 \Rightarrow I_{SS} \to S_{11} - S_{12}, \ I_\perp \to S_{11} + S_{21} - S_{12} - S_{22}, \tag{11}$$

where all Mueller matrix elements are considered at exact side scattering direction. The particular value of κ is not relevant since we will always consider either qualitative behavior of plots including I_{SS} and $I_\perp$ or relative values.

Next, we summarize the experimental conclusions of de Grooth, *et al.* [14], that we will explain by rigorous DDA simulations in Section 6. The scatter plot of the sample containing eosinophils and neutrophils in $I_\perp$ versus I_{SS} coordinates shows clear discrimination of two subtypes. The I_{SS} signals are almost the same, while $I_\perp$ are larger for eosinophils. Moreover, there is significant correlation between $I_\perp$ and I_{SS} for both neutrophils and eosinophils. Discrimination between two subtypes is the most pronounced using D_{SS}, with mean values of 0.044 and 0.013 for eosinophils and neutrophils respectively (averaged over a single sample). They also showed that D_{SS} is almost constant when $\Delta\varphi$ is decreased at fixed $\Delta\theta$ for both granulocyte subtypes. Thus, the depolarization signals of granulocytes are inherent in contrast to the aperture depolarization, e.g. of a sphere, which is caused by a finite value of the detector aperture around the exact side scattering direction and decreases to zero with decreasing $\Delta\varphi$.

4. The Rayleigh-Debye-Gans approximation

Consider our model of a granulated sphere (see Section 2). The position of the granule centers relative to the origin, which is placed in the cell center, is given by vectors $\mathbf{r}_i$, where i is from 1 to N, and N is total number of granules. V_c, x_c and V_g, x_g are the volume and the size parameter of the cell and one granule respectively, and the volume fraction of granules is given by $f = NV_g/V_c = N(x_g/x_c)^3$. We assume that granules are randomly positioned inside the cell, and they are not allowed to overlap. Furthermore, to simplify our derivations we assume that $x_g \ll x_c$. It is important to note that x_g can be both small and large compared to unity. We formulate the random granule position as: $\mathbf{r}_i$ is uniformly random inside the sphere with size parameter $x_c - x_g$. Thus we neglect the boundary effects due to the non-overlapping of granules, which are significant only for large f in the layer of width of order of d_g from the cell boundary. It is important to note that the pair distribution function of granules, which will be discussed below, is much more sensitive to the non-overlapping condition than the probability distribution function of a single granule position. The incident wave propagates along the z-axis and the scattering direction $\mathbf{n}$ is described by angles θ and φ. We consider the scattering problem of a particle in vacuum, i.e. we divide all relevant quantities by the refractive index of the host medium.

To understand the dependence of side-scattering intensity on the granule size we consider the RDG approximation [33]. We consider the limit of small refractive indices, i.e. $|m - 1| \ll 1$ for both cell cytoplasm and granules. Actually, RDG is strictly valid only when $x|m - 1| \ll 1$, which, strictly speaking, is not true for our particles. We will see, however, that it is capable of describing some features that are obtained by accurate DDA simulations.

Our goal is to derive simple analytical expression rather than to keep all derivations as accurate as possible. We can derive the final RDG result numerically with any required accuracy for any particular granule configuration and then perform numerical averaging over all possible configurations. This is a laborious task, albeit much faster than the DDA simulations. However, such brute-force numerical simulations of RDG-based theory are anyway not accurate enough. Therefore, we prefer to additionally sacrifice some accuracy to derive analytical expressions, which give added value compared to rigorous DDA simulations. This value consists in physical insight into the light scattering problem, e.g. scaling laws, and the opportunity for an approximate solution of the inverse light scattering problem. Although

we discuss all employed assumptions and approximations, the accuracy of the final expressions can only be determined by comparison with the DDA simulations.

According to the RDG theory, only the diagonal elements of the amplitude scattering matrix are nonzero [33]:

$$S_1(\mathbf{n}) = -\frac{ik^3}{2\pi}\sum_{i=0}^{N}(m_i-1)V_i h(V_i,\mathbf{n}), \; S_2(\mathbf{n}) = S_1(\mathbf{n})\cos\theta, \tag{12}$$

where the particle is divided into $N+1$ domains: $i=0$ corresponds to the cytoplasm and the rest to N granules. m_i and V_i are refractive index and volume of each domain. $h(V,\mathbf{n})$ is a form factor given by

$$h(V,\mathbf{n}) = \frac{1}{V}\int_V d^3 r \exp(i\mathbf{r}\cdot\mathbf{q}), \tag{13}$$

where we have introduced $\mathbf{q} = k(\mathbf{e}_z - \mathbf{n})$. The form factor for a sphere, which center is in the origin, can be obtained analytically [33]:

$$h_s(x,\theta) = g_s(u) = \frac{3}{u^3}(\sin u - u\cos u), u = qr = 2x\sin\frac{\theta}{2}, \tag{14}$$

where r and x are the radius and the size parameter of a sphere, and there is no dependency on the azimuthal angle. The asymptotic behavior of Eq. (14) is:

$$g_s(u) = \begin{cases} 1+\mathrm{O}(u^2), & u<1; \\ 3u^{-2}\cos u + \mathrm{O}(u^{-3}), & u>1. \end{cases} \tag{15}$$

Using the linearity of Eq. (12) in the factor $m-1$, we consider separately the spherical cytoplasm with factor m_c-1 and superimposed granules with factor $m_g - m_c$. Then, Eq. (12) can be rewritten as

$$S_1(\mathbf{n}) = -\frac{ik^3}{2\pi}\left[(m_c-1)V_c h_s(x_c,\theta)+(m_g-m_c)V_g h_s(x_g,\theta)\xi(N)\right], \tag{16}$$

where $\xi(N)$ holds all the dependency on granule positions:

$$\xi(N) = \sum_{i=1}^{N}\exp(i\mathbf{r}_i\cdot\mathbf{q}). \tag{17}$$

Averaging of $\xi(N)$ over all possible granule positions is performed independently for each element of the sum leading to the same integral as the one in Eq. (13), therefore

$$<\xi(N)> = Nh_s(x_c - x_g,\theta). \tag{18}$$

The second moment of the absolute value of $\xi(N)$ is given by:

$$<|\xi(N)|^2> = \sum_{i,j=1}^{N}<\exp(i(\mathbf{r}_i-\mathbf{r}_j)\cdot\mathbf{q})> = N + N(N-1)<\exp(i(\mathbf{r}_i-\mathbf{r}_j)\cdot\mathbf{q})>_{i\neq j}, \tag{19}$$

Now we consider a particular case by assuming that $\mathbf{r}_i$ and $\mathbf{r}_j$ are independent. In other words, we neglect the effect of the non-overlapping condition on the statistical properties of granule positions. This is only valid for sufficiently small volume fractions ($f \ll 1$). Then

$$<|\xi(N)|^2> = N + N(N-1)h_s^2(x_c - x_g,\theta), \tag{20}$$

Using Eqs. (18) and (20) one can obtain

$$\left\langle |S_1(\theta)|^2 \right\rangle = \left(\frac{2}{3}x_c^3\right)^2\Bigg(\left|(m_c-1)h_s(x_c,\theta)+f(m_g-m_c)h_s(x_g,\theta)h_s(x_c-x_g,\theta)\right|^2$$
$$+\left|f(m_g-m_c)h_s(x_g,\theta)\right|^2\left[1-h_s^2(x_c-x_g,\theta)\right]/N\Bigg). \tag{21}$$

Equation (21) is obtained under the assumptions $x_g \ll x_c$ and $f \ll 1$ (and the RDG approximation itself). In particular, if the limit $x_g \to 0$ and $N \to \infty$ is taken, keeping f constant, then

$$\left\langle \left| S_1(\theta) \right|^2 \right\rangle = \left| \frac{2}{3} x_c^3 (m_e - 1) h_s(x_c, \theta) \right|^2, \ m_e = f m_g + (1 - f) m_c, \tag{22}$$

which is exactly an RDG result for a homogeneous sphere with effective refractive index m_e. the expression for m_e can be considered as a simplified Maxwell-Garnett EMT in the limit of both m_g and m_c being close to unity. If we consider typical parameters of our problem: $m_c = 1.015$, $m_g = 1.2$, $\lambda = 0.4936$ μm, $D_c = 8$ μm, then even for the smallest x_g and f that we simulated ($x_g = 0.48 \Leftrightarrow d_g = 75$ nm, $f = 0.02$) the first term in Eq. (21) (the one that is independent of N) is about an order of magnitude smaller than the second. Therefore, we may completely neglect the cytoplasm except for its total volume and the effect it has on the refractive index of the granules. By that we introduce an assumption $x_c \gg 1$, and use it for a new evaluation of Eqs. (18) and (19) discarding the condition $f \ll 1$. Granules are uniformly distributed inside a large volume with volume fraction f, without overlapping. Taking the limit of infinitely large volume ($N \to \infty$, $f = $ const) and finite θ ($\theta \sim 1$), that is equivalent to a model of a hard spheres liquid, for which it is known that [37,38]

$$< \xi(N) > = 0, \ < |\xi(N)|^2 > = N S_f(q); \tag{23}$$

S_f is a structure factor, for which an explicit albeit cumbersome expression is known [37]:

$$\frac{1}{S_f(q)} = \frac{1}{g_f(v)} = 1 + \frac{24f}{v^3} \left\{ a_f (\sin v - v \cos v) + b_f \left[\left(\frac{2}{v^2} - 1 \right) v \cos v + 2 \sin v - \frac{2}{v} \right] \right.$$

$$\left. + \frac{f a_f}{2} \left[\frac{24}{v^3} + 4 \left(1 - \frac{6}{v^2} \right) \sin v - \left(1 - \frac{12}{v^2} + \frac{24}{v^4} \right) v \cos v \right] \right\}, \tag{24}$$

$$v = q d_g = 4 x_g \sin(\theta/2), \ a_f = \frac{(1 + 2f)^2}{(1 - f)^4}, \ b_f = -\frac{3}{2} \frac{f(2 + f)^2}{(1 - f)^4}. \tag{25}$$

.Employing the assumptions discussed above together with Eqs. (16), (23) one may obtain

$$\left\langle \left| S_1(\theta) \right|^2 \right\rangle = \left| \frac{2}{3} x_c^3 f (m_g - m_c) h_s(x_g, \theta) \right|^2 S_f(q)/N. \tag{26}$$

Derivation of Eq. (26) under the assumption $x_c \gg 1$ is similar to that performed in §3.3 of [39]. The final quantity of interest is the total side scattering intensity [cf. Eqs. (8) and (10)]:

$$I_{SS} = \frac{1}{4\Delta\theta\Delta\varphi} \int\limits_{\pi/2-\Delta\theta}^{\pi/2+\Delta\theta} \int\limits_{\pi/2-\Delta\varphi}^{\pi/2+\Delta\varphi} d\varphi\, d\theta (S_{11} + S_{12} \cos 2\varphi + S_{13} \sin 2\varphi)$$

$$= \frac{1}{8\Delta\theta\Delta\varphi} \int\limits_{\pi/2-\Delta\theta}^{\pi/2+\Delta\theta} \int\limits_{\pi/2-\Delta\varphi}^{\pi/2+\Delta\varphi} d\varphi\, d\theta |S_1(\mathbf{n})|^2 \left((1 + \cos^2\theta) + (\cos^2\theta - 1)\cos 2\varphi \right), \tag{27}$$

where Eq. (12) was used. Since averaging and integration can be interchanged,

$$\left\langle I_{SS} \right\rangle = \frac{1}{4\Delta\theta} \int\limits_{\pi/2-\Delta\theta}^{\pi/2+\Delta\theta} d\theta \left((1 + \cos^2\theta) + (1 - \cos^2\theta) \frac{\sin 2\Delta\varphi}{2\Delta\varphi} \right) \left\langle |S_1(\theta)|^2 \right\rangle. \tag{28}$$

Using Eq. (26), this integral can be computed numerically for any set of parameters. It is interesting to analyze the scaling of RDG results. For that we rewrite Eq. (28) as

$$\left\langle I_{SS} \right\rangle = \frac{4}{9} x_c^3 f \left| m_g - m_c \right|^2 h_{SS}(x_g, f), \tag{29}$$

where $h_{SS}(x, f)$ is the following function:

$$h_{SS}(x,f) = \frac{x^3}{4\Delta\theta} \int_{\pi/2-\Delta\theta}^{\pi/2+\Delta\theta} d\theta \left((1+\cos^2\theta) + (1-\cos^2\theta)\frac{\sin 2\Delta\varphi}{2\Delta\varphi} \right) h_s^2(x,\theta) S_f(q). \tag{30}$$

First, we analyze the scaling behavior of $g_f(v)$. One may show that

$$g_f(v) = \begin{cases} \dfrac{(1-v)^4}{(1+2v)^2} + O(v^2), & v < 1; \\[2mm] 1 + O(v^{-2}), & v > 1, \end{cases} \tag{31}$$

and finally:

$$h_{SS}(x,f) = \begin{cases} C_1^{ap} \dfrac{(1-f)^4}{(1+2f)^2} x^3 + O(x^5), & x < 1; \\[2mm] C_2^{ap}(x) x^{-1} + O(x^{-2}), & x > 1, \end{cases} \tag{32}$$

where constants $C_{1,2}^{ap}$ are determined by the aperture angles $\Delta\theta$ and $\Delta\varphi$. C_2^{ap} also weakly depends on x, but this is ignored in this discussion.

5. The second-order Born approximation

To theoretically approach the depolarized intensity we employ the second order of the RDG or, more precisely, the second-order Born (2-Born) approximation. We use the same definitions as given in Section 4, and the same philosophy of preferring simplicity to the best possible accuracy. The internal field inside the scatterer is a sum of two orders (see e.g. [10]):

$$\mathbf{E}(\mathbf{r}) = \mathbf{E}^{(0)}(\mathbf{r}) + \mathbf{E}^{(1)}(\mathbf{r}), \ \mathbf{E}^{(0)}(\mathbf{r}) = \mathbf{E}^{inc}(\mathbf{r}), \tag{33}$$

$$\mathbf{E}^{(1)}(\mathbf{r}) = \int_{V_c \backslash V_0} d^3 r' \overline{\mathbf{G}}(\mathbf{r},\mathbf{r}')\chi(\mathbf{r}')\mathbf{E}^{(0)}(\mathbf{r}') - \frac{4\pi}{3}\chi(\mathbf{r})\mathbf{E}^{(0)}(\mathbf{r}), \tag{34}$$

where $\mathbf{E}^{inc}(\mathbf{r})$ and $\mathbf{E}(\mathbf{r})$ are the incident and total electric field, $\chi(\mathbf{r}) = (m^2(\mathbf{r}) - 1)/4\pi$ is the susceptibility of the medium, V_0 is an infinitesimally small spherical exclusion volume around $\mathbf{r}$. $\overline{\mathbf{G}}(\mathbf{r},\mathbf{r}')$ is the free space dyadic Green's function, defined as

$$\overline{\mathbf{G}}(\mathbf{r},\mathbf{r}') = \frac{\exp(ikR)}{R}\left[k^2\left(\overline{\mathbf{I}} - \frac{\hat{R}\hat{R}}{R^2}\right) - \frac{1-ikR}{R^2}\left(\overline{\mathbf{I}} - 3\frac{\hat{R}\hat{R}}{R^2}\right)\right], \tag{35}$$

where $\overline{\mathbf{I}}$ is the identity dyadic, $k = \omega/c$ is the free space wave vector, $\mathbf{R} = \mathbf{r} - \mathbf{r}'$, $R = |\mathbf{R}|$, and $\hat{R}\hat{R}$ is a dyadic defined as $\hat{R}\hat{R}_{\mu\nu} = R_\mu R_\nu$ (μ and ν denote Cartesian coordinates).

Most of the scattering quantities can be obtained from the scattering amplitude [33]:

$$\mathbf{F}(\mathbf{n}) = -ik^3(\overline{\mathbf{I}} - \hat{n}\hat{n})\int_{V_c} d^3 r' \exp(-ik\mathbf{r}'\cdot\mathbf{n})\chi(\mathbf{r}')\mathbf{E}(\mathbf{r}'). \tag{36}$$

To simplify our derivations we consider the depolarized intensity $I_\perp^{(0)}$ for zero aperture ($\Delta\theta = \Delta\varphi = 0°$), i.e. we study only the intrinsic part, which is not caused by the finite value of the aperture. Then

$$I_\perp^{(0)} = \left| S_3(\mathbf{e}_y) \right|^2, \tag{37}$$

while $S_3(\mathbf{e}_y) = F_z(\mathbf{e}_y)$ for the incident field equal to

$$\mathbf{E}^{inc}(\mathbf{r}) = \mathbf{e}_x \exp(ikr_z). \tag{38}$$

It is easy to show that both $\mathbf{E}^{(1)}(\mathbf{r})$ and the last term in Eq. (34) results in zero contribution to

$S_3(\mathbf{e}_y)$, from which it follows that

$$S_3(\mathbf{e}_y) = -\mathrm{i}k^3 \int\limits_{V_c \backslash V_0} \int\limits_{V_c} \mathrm{d}^3 r' \mathrm{d}^3 r \exp(\mathrm{i}k(r_z - r_y')) \chi(\mathbf{r}') \chi(\mathbf{r}) G_{zx}(\mathbf{r},\mathbf{r}'). \tag{39}$$

Like in the RDG derivations, we divide the scatterer into the whole volume V_c with susceptibility χ_c and superimposed granules with total volume V_{grs} and susceptibility $\chi_g - \chi_c$). The integral in Eq. (39) is decomposed into four parts: a double integral over V_c, a double integral over V_{grs} and two cross-terms (over V_c and V_{grs}). The first term is just a second-order Born approximation for a homogenous sphere, which identically equals zero because of symmetry (S_3 is always zero for a sphere). The cross-terms are very similar and they both can be thought of as RDG scattering by V_{grs} for an incident field produced by the RDG applied to V_c. One can show that the RDG applied to an index-matching homogenous sphere much larger than the wavelength produces an internal field parallel to the incident one, except at a distance of order of wavelength from the boundary. The x-component of the internal field does not contribute to the depolarization at exact side scattering direction. Therefore, the relative contribution of the cross-terms in Eq. (39) is at least an order of $(m_c - 1)/[fx_c(m_g - m_c)]$ smaller than the remaining granule-granule interaction, and can be neglected. Moreover, interaction of a granule with itself results in identically zero polarization. Hence,

$$S_3(\mathbf{e}_y) = -\mathrm{i}\frac{k^3}{4\pi^2}(m_g - m_c)^2 \sum_{\substack{i,j=1 \\ i \neq j}}^{N} \int\limits_{V_i} \int\limits_{V_j} \mathrm{d}^3 r' \mathrm{d}^3 r \exp(\mathrm{i}k(r_z - r_y')) G_{zx}(\mathbf{r},\mathbf{r}'). \tag{40}$$

Averaging Eq. (37) over all possible sets of granule positions results in

$$\left\langle I_\perp^{(0)} \right\rangle = \frac{k^6}{16\pi^4}|m_g - m_c|^4 \sum_{\substack{i,j=1 \\ i \neq j}}^{N} \sum_{\substack{i',j'=1 \\ i' \neq j'}}^{N} \int\limits_{V_g} \int\limits_{V_g} \int\limits_{V_g} \int\limits_{V_g} \mathrm{d}^3 r''' \mathrm{d}^3 r'' \mathrm{d}^3 r' \mathrm{d}^3 r \exp\left(\mathrm{i}k(r_z - r_z'' + r_y''' - r_y')\right) \times$$

$$\times \left\langle G_{zx}(\mathbf{r},\mathbf{R}_{ij}+\mathbf{r}') G_{zx}^*(\mathbf{r}'',\mathbf{R}_{i'j'}+\mathbf{r}''') \exp\left(\mathrm{i}k(R_{i,z} - R_{i',z} + R_{j,y} - R_{j,y})\right) \right\rangle, \tag{41}$$

where $*$ denotes complex conjugate, $\mathbf{R}_{ij} = \mathbf{r}_j - \mathbf{r}_i$, and integration is performed over a granule positioned in the origin. If all four indices: i, j, i', and j' are different then $\mathbf{R}_{ij}$ and $\mathbf{R}_{i'j'}$ are independent. We assume that $\mathbf{R}_{ij}$ and $\mathbf{R}_{ij'}$ ($j \neq j'$) are also independent; by that we neglect the triple correlations. In case arguments of two Green's tensors in Eq. (41) are independent, they can be averaged independently. The result is then zero because changing sign of the x component of $\mathbf{R}_{ij}$ inverts the sign of $G_{zx}(\mathbf{R}_{ij})$ while not affecting any of the exponents in Eq. (41). Therefore, we need to consider only the terms with either (1) $i = i'$ and $j = j'$ or (2) $i = j'$ and $j = i'$. All the instantiations of (1) are equivalent, and so are the instantiations of (2). Therefore,

$$\left\langle I_\perp^{(0)} \right\rangle = \frac{k^6}{16\pi^4}|m_g - m_c|^4 N^2 \left\langle \left|H(\mathbf{R}_{ij})\right|^2 \left[1 + \exp(\mathrm{i}k(\mathbf{e}_z + \mathbf{e}_y) \cdot \mathbf{R}_{ij})\right] \right\rangle_{i \neq j}, \tag{42}$$

$$H(\mathbf{R}) = \int\limits_{V_g} \int\limits_{V_g} \mathrm{d}^3 r' \mathrm{d}^3 r \exp\left(\mathrm{i}k(r_z - r_y')\right) G_{zx}(\mathbf{r},\mathbf{R}+\mathbf{r}'), \tag{43}$$

where $N \gg 1$ is assumed.

To keep the derivations analytical in calculation of $H(\mathbf{R}_{ij})$ we assume that $R_{ij} \gg d_g$. However, the following derivation is expected to be approximately correct also for small R_{ij}, resulting in the correct scaling laws but with different constants. Employing the assumption of distant granules we obtain

$$H(\mathbf{R}) = G_{zx}(\mathbf{R}) \int\limits_{V_g} \int\limits_{V_g} \mathrm{d}^3 r' \mathrm{d}^3 r \exp\left(\mathrm{i}k[r_z - r_y' + (\mathbf{r}' - \mathbf{r}) \cdot \mathbf{n}]\right)$$

$$= V_g^2 G_{zx}(\mathbf{R}) g_s(x_g|\mathbf{n} - \mathbf{e}_z|) g_s(x_g|\mathbf{n} - \mathbf{e}_y|), \tag{44}$$

where $g_s(u)$ is defined by Eq. (15) and $\mathbf{n} = \mathbf{R}/R$ is a unit direction vector. Using Eq. (44) and the fact that

$$\left|G_{zx}(\mathbf{R})\right|^2 = n_z^2 n_x^2 h_{\mathrm{G}}(R), \; h_{\mathrm{G}}(R) = \frac{9 + 3(kR)^2 + (kR)^4}{R^6}, \tag{45}$$

Eq. (42) can be rewritten as

$$\left\langle I_{\perp}^{(0)} \right\rangle = \frac{k^6}{16\pi^4} \left| m_{\mathrm{g}} - m_{\mathrm{c}} \right|^4 N^2 V_{\mathrm{g}}^4 \int \mathrm{d}R \; P(R) h_{\mathrm{G}}(R) h_{\Omega}(x_{\mathrm{g}}, R), \tag{46}$$

where $P(R)$ is a radial distribution function of relative granule positions, defined so that $\int \mathrm{d}R \, P(R) = 1$, and h_{Ω} is the following result of averaging over the whole solid angle, since all $\mathbf{n}$ are equiprobable,

$$h_{\Omega}(x, R) = \frac{1}{4\pi} \oint \mathrm{d}^2 n \, n_z^2 n_x^2 [1 + \cos(kR(n_z + n_y))] \, g_{\mathrm{s}}^2(x|\mathbf{n} - \mathbf{e}_z|) g_{\mathrm{s}}^2(x|\mathbf{n} - \mathbf{e}_y|). \tag{47}$$

The exponent in Eq. (42) was replaced by a cosine function because the imaginary part of h_{Ω} is zero due to the symmetry properties of the integrand.

It is easy to show that $P(R)$ for *point* granules in a sphere of diameter D_{c} is given by

$$P(R) = \frac{6}{D_{\mathrm{c}}^5} R^2 (D_{\mathrm{c}} - R)^2 (2D_{\mathrm{c}} + R), \tag{48}$$

independent of *f*. Taking into account a finite size of granules, which is assumed much smaller than D_{c}, modifies $P(R)$ only for R close to 0 and D_{c}. Moreover, we neglect the boundary effects for large R, because the contribution to the integral in Eq. (46) from a small interval near D_{c}, which has width of order d_{g}, is relatively small. The correction for small R can be obtained in the limit of infinitely large D_{c}, i.e. considering a granulated sphere as an infinite hard sphere liquid ($x_{\mathrm{c}} \gg 1$ and $x_{\mathrm{c}} \gg x_{\mathrm{g}}$). The structure factor given by Eq. (24) is basically a Fourier transform of $P(R)$ [37], hence $P(R)$ can be obtained by the inverse Fourier transform

$$P(R) = \frac{24 R^2}{D_{\mathrm{c}}^3} \left(1 + \frac{d_{\mathrm{g}}^3}{12\pi f} \int_0^\infty \mathrm{d}q [S_f(q) - 1] q^2 \frac{\sin(qR)}{qR} \right). \tag{49}$$

This integral cannot be computed in closed analytical form. Therefore, we expand $S_f(q)$ in series of *f* and leave only terms up to the second order, since higher orders anyway cannot be computed accurately without consideration of triple- and higher scattering orders. After that one may obtain the final result for $P(R)$:

$$P(R) = \begin{cases} \dfrac{24 R^2}{D_{\mathrm{c}}^3} \left(1 + f \dfrac{(2d_{\mathrm{g}} - R)^2 (4d_{\mathrm{g}} + R)}{2d_{\mathrm{g}}^3} \right), & d_{\mathrm{g}} \le R \le 2d_{\mathrm{g}}; \\[2ex] \dfrac{6}{D_{\mathrm{c}}^5} R^2 (D_{\mathrm{c}} - R)^2 (2D_{\mathrm{c}} + R), & R > 2d_{\mathrm{g}}. \end{cases} \tag{50}$$

Using Eqs. (45), (47), and (50), the integral in Eq. (46) can be computed; however, it is still cumbersome. To simplify, we notice that h_{Ω} only weakly depends on R, while different parts of $h_{\mathrm{G}}(R)$ exhibit very different scaling with respect to R [cf. Eq. (45)]. The first two terms increase when $R \to 0$ [after multiplication by $P(R)$], and the integral is determined by a small interval of R, up to several d_{g}. On the contrary, the third part of $h_{\mathrm{G}}(R)$ has a smooth behavior, and it's integral is determined by the whole range of R. In particular, when evaluating the integral of the third part of $h_{\mathrm{G}}(R)$ the cosine term in h_{Ω} can be neglected, since for $kR \gg 1$, which is valid for most of the R range, the contribution of this term is negligible compared to the unity addend. We denote the resulting h_{Ω} as $h_{\Omega}(x, \infty)$, and one may show that

$$h_{\Omega}(x, \infty) = \begin{cases} \dfrac{1}{15} \left(1 - \dfrac{4}{5} x^2 + \mathrm{O}(x^4) \right), & x < 1; \\[2ex] \mathrm{O}(x^{-8} \ln x), & x > 1, \end{cases} \tag{51}$$

$$h_{\Omega}(x, R) \le 2 h_{\Omega}(x, \infty). \tag{52}$$

Contribution of the third part of $h_G(R)$ to the integral in Eq. (46) is

$$\int dR\, P(R)\frac{k^4}{R^2}h_\Omega(x_g,R) = \frac{18k^3 x_c h_\Omega(x_g,\infty)}{D_c^3}.\tag{53}$$

Next we calculate the contribution of the first two parts of $h_G(R)$. As we will show below, this contribution is significant only for small x_g. Therefore, we expand $h_\Omega(x_g,R)$ in series of x_g, similar to Eq. (51), assuming $kR = O(x_g)$:

$$h_\Omega(x_g,R) = \frac{2}{15}\left(1-\frac{4}{5}x_g^2-\frac{1}{7}(kR)^2+O(x_g^4)\right).\tag{54}$$

Using Eqs. (50), (54) we obtain

$$\int dR\, P(R)\frac{9+3(kR)^2}{R^6}h_\Omega(x_g,R)$$
$$=\frac{6k^3}{5D_c^3 x_g^3}\left[1+\frac{f}{4}(1+6\ln 2)+\frac{x_g^2}{35}(52+f(373-522\ln 2))+O(x_g^4,f^2)\right].\tag{55}$$

It is important to note, that Eq. (55) is not completely accurate, because it is determined by $R \sim d_g$, for which derivation of Eq. (44) is not accurate. Comparing Eq. (55) to Eqs. (53) and (51) one can see that the contribution of the third part of $h_G(R)$ is negligible for very small x_g but becomes dominating, compared to other parts, for x_g larger than a few times $x_c^{-1/3}$. This conclusion can be derived rigorously for the whole range of x_g, using Eq. (52) instead of Eq. (54) for evaluation of the integral in Eq. (55). Physically speaking, for very small granules the depolarized intensity is determined by the short-range interaction of granules that happen to be close to each other. Starting from $x_g \sim x_c^{-1/3}$ the main contribution is from the long-range interaction of all granules. Therefore, we may use Eq. (55) for x_g up to some arbitrary chosen constant of order less than unity (we choose it to be unity), and set its contribution to zero for larger x_g. Fortunately, this exactly corresponds to the assumptions that were used in obtaining Eq. (55). The final result for depolarization intensity is

$$\left\langle I_\perp^{(0)}\right\rangle = \frac{4}{135}\left|m_g-m_c\right|^4 f^2 x_c^3 x_g^3\left[C_\perp(x_g,f)+x_g^3 x_c h_\Omega(x,\infty)\right],\tag{56}$$

$$C_\perp(x,f) = \begin{cases}1+\dfrac{f}{4}(1+6\ln 2)+\dfrac{x^2}{35}(52+f(373-522\ln 2)), & x<1;\\[2mm] 0, & x\geq 1.\end{cases}\tag{57}$$

Using Eqs. (29) and (56) one may derive the scaling behavior of depolarization ratio:

$$D_{SS}(x_g) = f\left|m_g-m_c\right|^2\times\begin{cases}C_D+O(f)+O(x_c x_g^3), & x_g\ll 1;\\[2mm] x_c O(x_g^{-1}\ln x_g), & x_g\gg 1,\end{cases}\tag{58}$$

Although our derivations do predict $O(f^2)$ corrections of D_{SS} for small x_g, this correction is not accurate because of higher-order scattering effects which are of the same order. The factor $O(x_g^{-1}\ln x_g)$ is almost constant for a range of large x_g that we studied, so we may consider both limiting values of D_{SS} to be independent of x_g. Hence, our approximate derivations based on the RDG and the 2-Born predicts the step-wise behavior of $D_{SS}(x_g)$.

The 2-Born also can be used to refine the RDG results for I_{SS}. Although this definitely improves the accuracy, it also makes the final result significantly more complex. Derivation for the exact side scattering direction is more cumbersome than that for $I_\perp$, because less terms in intermediate equations cancel out. Averaging over the side scattering aperture also does not seem feasible in closed form. Therefore this refinement contradicts our philosophy for approximate theories and we do not pursue it further.
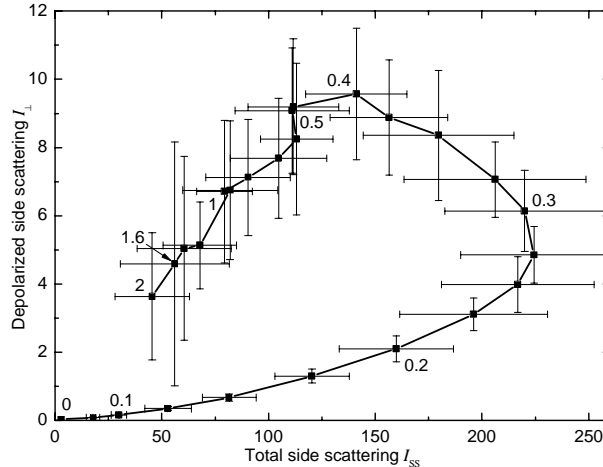
Fig. 2. Depolarized versus total side scattering intensities for several granule diameters from 0 to 2 μm, indicated for some points by labels, for the default set of parameters (see text). Mean values ± 2×SD are shown.

6. Results and discussion

The results of DDA simulations of side scattering by granulated spheres with the default set of parameters and varying granule diameter is shown in Fig. 2. For each d_g mean values of I_{SS} and $I_\perp$ and error bars corresponding to two SDs are shown. Labels near some of the points indicate the values of d_g. One can see that there are two ranges of d_g: from 0.1 to 0.25 μm and from 0.4 to 2 μm, which correspond to distinct regions in Fig. 2. The range from 0.25 to 0.4 μm is intermediate, where I_{SS} and $I_\perp$ strongly albeit differently depend on d_g. The two regions in Fig. 2 qualitatively correspond to the neutrophils and eosinophils on the plots by de Grooth *et al.* [14]. Considering the morphological characteristics of neutrophil and eosinophils granules, the difference in depolarized side scattering can be explained solely by the difference in d_g. However, it is important to note, that direct comparison cannot be performed because the model is a significant simplification of the granulocyte morphology. Apart from neglecting a nucleus, it assumes the same size for all granules, while granule population of a real granulocyte is always heterogeneous both in size and refractive index.

The results for several volume fractions are shown in Fig. 3, separately for I_{SS}, $I_\perp$, and their ratios. One may note that EMT result ($d_g = 0$) for D_{SS} seems to be different from the limiting value of the DDA simulations [Fig. 3(c)]. This is explained by the fact that both I_{SS} and $I_\perp$ are mostly determined by the granules even for the smallest $d_g = 0.075$ μm that we tried. However, for much smaller granules the signals are those of the homogeneous sphere, which has a different depolarization mechanism (see Fig. 5 and Section 5). Therefore, both I_{SS} and $I_\perp$ decrease monotonically with d_g, while D_{SS} "switches" from the limiting value of small granules to that of a homogeneous sphere, which are naturally different.

Apart from this feature, the general behavior of I_{SS}, $I_\perp$, and D_{SS} versus d_g, is similar to that predicted by Eqs. (29), (56), and (58): both I_{SS} and $I_\perp$ rapidly increase with d_g for small d_g and relatively slowly decay for larger d_g. D_{SS} behaves in a step-like manner, switching from a plateau for small d_g to another one for larger d_g. We include the literature data on average values of D_{SS} for neutrophils and eosinophils [14] in Fig. 3(c). One can see that neutrophils approximately correspond to small d_g limit for $f = 0.1$, while eosinophils have the D_{SS} values between the large and small d_g limits for the same f. The latter can be explained by the fact that eosinophils have large (> 0.4 μm), small (< 0.25 μm), and intermediate granules, and $f = 0.1$ is their typical total volume fraction. It is important to note, that this explanation is
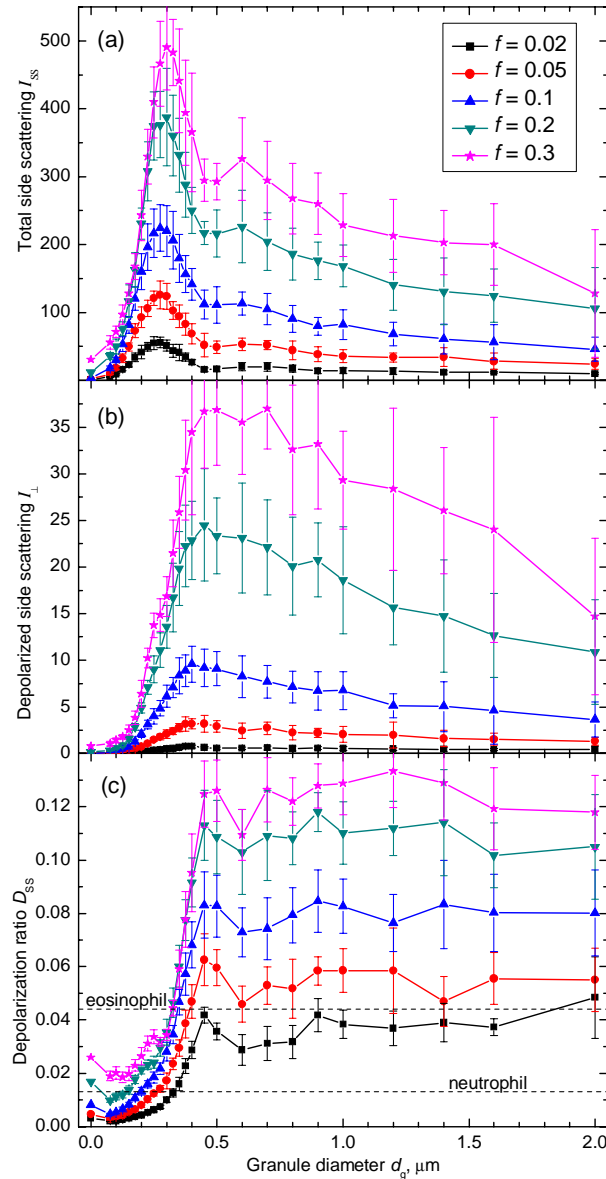
Fig. 3. (a). Total and (b) depolarized side scattering intensity and (c) their ratio versus granule diameter for several volume fractions. Other parameters are set to default values (see text). Mean values $\pm 2 \times$SD are shown. Experimental results for mean values of D_{SS} of neutrophils and eosinophils are shown in (c) for comparison.

only qualitative, because light scattering signals for a cell with granules of different sizes cannot be obtained by averaging of results for different cells with identical granules. The quantitative comparison between the DDA simulations and experimental results for D_{SS} is further hindered by the uncertainty of m_g.

To show the dependence of side scattering signals on f we plot $I_\perp$ versus I_{SS} in Fig. 4, normalizing them by f^2 and f respectively [cf. Eqs. (29) and (56)]. We omit error bars in Figs. 4–7 for clarity. In all cases they are similar to those depicted in Figs. 2 and 3. The only exception is Fig. 5, for which SD significantly increase with decreasing $\Delta\varphi$ (data not shown). This increase is natural considering the oscillating dependence of all Mueller matrix elements
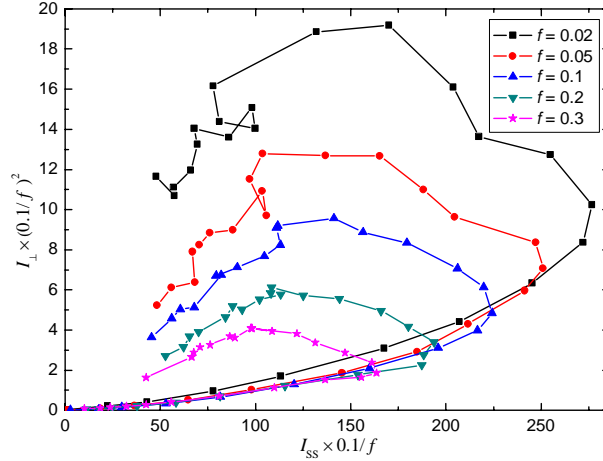
Fig. 4. Same as Fig. 2 but for several volume fractions. $I_\perp$ and I_{SS} are normalized by f^2 and f respectively to the case $f = 0.1$.
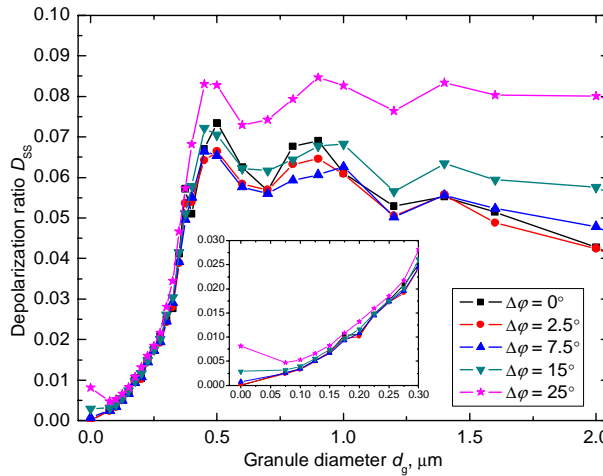

Fig. 5. Mean values of depolarization ratio versus granule diameter for several sizes of azimuthal angle aperture. Other parameters, including $\Delta\theta$, are set to default values (see text). An inset shows the magnified region near the origin.

on both θ and φ. Analyzing Figs. 3 and 4, one can see that the scaling of $I_\perp$ and I_{SS} with f is slower than f^2 and f respectively, i.e. the corrections of higher order in f are important. Although our derivations do provide such corrections they are not expected to be accurate and therefore are not further discussed (see Sections 4 and 5). One also can see that the slope of the curves in Fig. 4 is almost independent on f for small d_g, hence D_{SS} is proportional to f in this regime. This scaling law holds with much better accuracy than that for either $I_\perp$ or I_{SS}.

We show the results of varying the aperture in Fig. 5. We keep $\Delta\theta$ fixed and vary $\Delta\varphi$ from $0°$ to $25°$. The depolarization ratio does depends on $\Delta\varphi$ over the whole range of d_g, however this dependence is uniform in the sense, that variation of $\Delta\varphi$ do not change the general behavior of D_{SS} versus d_g. In other words, the aperture part of the depolarization of the granulated sphere is significant, especially for large d_g, however it is always less than the inherent part. There is one natural exception to the above conclusion – the EMT result for $d_g = 0$, which scales approximately as $\Delta\varphi^2$ [14].

A plot of $I_\perp$ versus I_{SS} for several D_c is shown in Fig. 6, normalized by D_c^4 and D_c^3 respectively [cf. Eqs. (29) and (56)]. One may see that plots almost coincide for small d_g and
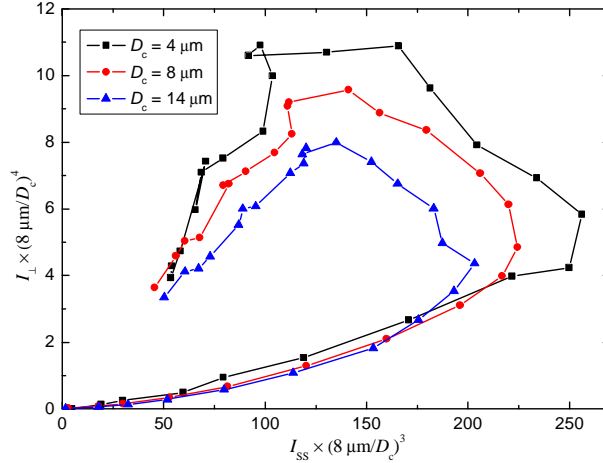
Fig. 6. Same as Fig. 2 but for several cell diameters. $I_\perp$ and I_{SS} values are normalized by D_c^4 and D_c^3 respectively to the case $D_c = 8$ μm.
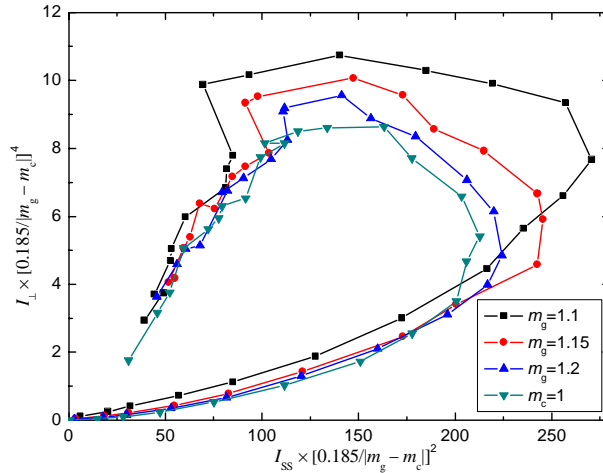

Fig. 7. Same as Fig. 2 but for several m_g with $m_c = 1.015$ and for $m_g = 1.2$, $m_c = 1$. $I_\perp$ and I_{SS} are normalized by $|m_g - m_c|^4$ and $|m_g - m_c|^2$ respectively to the case $m_g = 1.2$, $m_c = 1.015$.

come close to each other for large d_g. That means that the simple scaling derived from the approximate theories works satisfactory. Moreover, this scaling law is even more accurate for D_{SS}. The results for several m_g and m_c, shown in Fig. 7, lead to analogous conclusions: scaling described by approximate theories works well, especially for D_{SS}, except for the "resonance" intermediate region of d_g. In particular, this scaling can be used to estimate the effect of uncertainty in m_g and m_c on the final simulated results.

All the results above are for several side scattering signals. In Fig. 8 results for other scattering quantities are shown, namely Q_{ext} and $<\cos\theta>$. One can see that these quantities only moderately depend on a particular granule placement, as indicated by relatively small SDs. However, they non-trivially depend on both d_g and f. For small d_g, Q_{ext} is close to that of a homogeneous sphere with EMT refractive index, which linearly depends on f. Since dependence of Q_{ext} of a sphere on m is oscillating, so is the dependence of Q_{ext} of a granulated sphere on f for small d_g. For large d_g overall extinction by granules is less dependent on each other, therefore Q_{ext} increases with f for constant d_g (if $f = 0$, $Q_{ext} = 1.04$). In intermediate region of d_g Q_{ext} smoothly changes from one limiting value to another. The asymmetry parameter can be thought of as another measure of side scattering intensity. And one can see
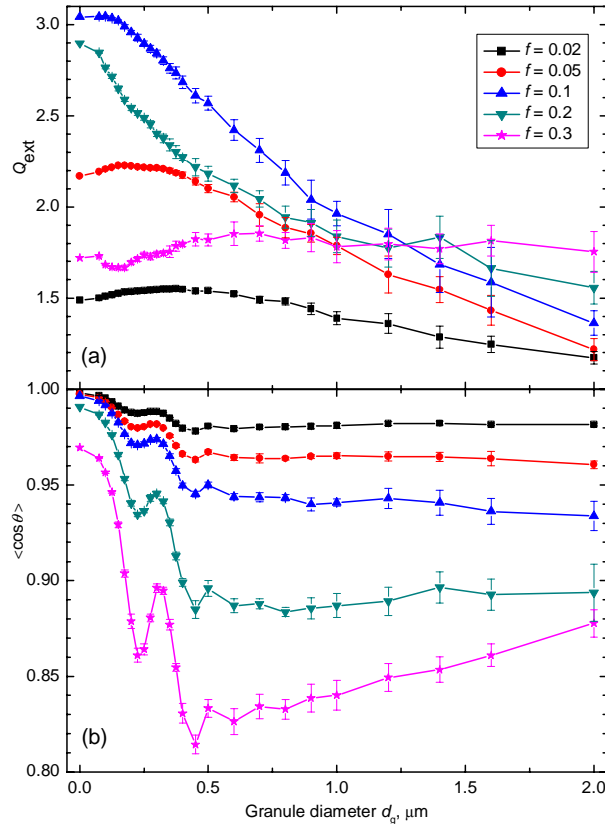
Fig. 8. Same as Fig. 3 but for (a) extinction efficiency and (b) asymmetry parameter.

that $1 - <\cos\theta>$ do correlate with I_{SS} when varying both d_g and f [cf. Figs. 3(a) and 8(b)]. However, the dependence of $<\cos\theta>$ on d_g has more oscillations (maxima and minima) than that of I_{SS}. Although some of the features of Fig. 8 are easy to understand, it does not seem feasible to completely describe this Fig. by any simple approximate theory.

We do not discuss other scattering quantities, e.g. angle-resolved Mueller matrix elements, in this manuscript, because it is hard to choose any of universal interest. Any particular application needs its own combination of Mueller matrix elements and range of scattering angles.

As we have seen above, RDG and 2-Born adequately describe the scaling of the side scattering signals. It is much more enlightening to perform a quantitative comparison of these approximate theories with DDA results. We present an example of such comparison in Fig. 9 for the default parameters of the DDA simulations (see Section 2). RDG results are shown for three volume fractions $f = 0.02$, 0.05, and 0.1, while 2-Born only for the default one ($f = 0.1$). One can see that RDG is an accurate approximation for small f, especially for small x_g. However, it systematically underestimates I_{SS} for larger f. This discrepancy is due to multiple scattering effects which are significant for larger f and are completely ignored in the framework of RDG. The RDG also has some more pronounced limitations, for example, the RDG result for Q_{ext} do not depend on x_g but only on f, contrary to the DDA simulations [see Fig. 8(a)]. Probably, RDG is more accurate for $<\cos\theta>$, but it cannot be accurately calculated in the framework described in Section 4 because of the employed assumption of not small θ.

It is important to note that 2-Born results shown in Fig. 9(b) [Eq. (56)] are obtained for zero scattering aperture, while DDA results are for $\Delta\theta = \Delta\varphi = 25°$. We do not use DDA results for zero aperture because their standard deviations are larger than the values themselves. Since we calculated only 10 different realizations of granule positions for each x_g,
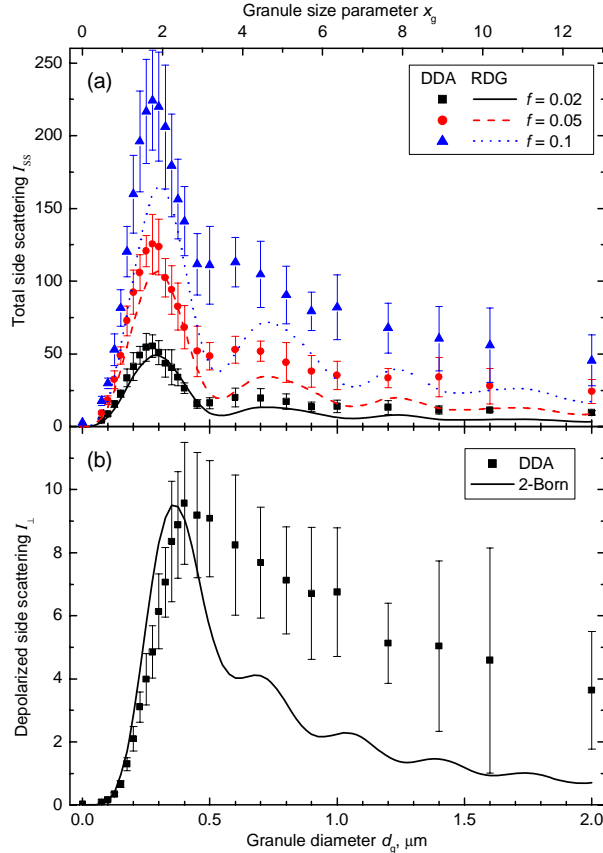
Fig. 9. Comparison of DDA results (mean $\pm$ 2$\times$SD) and mean values obtained (a) by the RDG for total- and (b) by second-order Born approximation for depolarized side scattering intensity. Typical parameters were used (described in the text) and for RDG – several values of f. Axes corresponding to both x_g and d_g are shown for convenience.

the errors of mean value are also large. One can see that the agreement between the 2-Born and the DDA is good, especially up to the first maximum. For larger x_g the 2-Born systematically underestimates the depolarized intensity, which is due to the neglect of higher-order scattering and the fact that even a single large granule is treated inaccurately in the framework of 2-Born.

7. Conclusion

We performed extensive DDA simulations of light scattering by a granulated sphere. We calculated total and depolarized side scattering intensity (I_{SS} and $I_{\perp}$) varying parameters of the model: granule diameter d_g, volume fraction f, and refractive index m_g, cytoplasm diameter and refractive index and size of the side scattering aperture. Parameters used correspond to the literature data on granulocyte morphology. The general appearance of the maps I_{SS} versus $I_{\perp}$ for several d_g is the same for different values of other model parameters: two segments with high correlation between I_{SS} and $I_{\perp}$ for small and large d_g and a connecting region for a narrow range of d_g. Both I_{SS} and $I_{\perp}$ increase with d_g for small d_g, have a maximum at d_g approximately equal to the wavelength λ, and slowly decay afterwards. Depolarization ratio D_{SS} behaves in a step-wise manner, having almost constant value for small d_g and a larger constant value for larger d_g.

Analytical expressions, obtained in the framework of the Rayleigh-Debye-Gans and second-order Born approximations, describe these results qualitatively well. Moreover, these

expressions quantitatively agree with rigorous DDA simulations for small d_g and f. In addition to being extremely fast, these approximate theories give an insight into the light scattering phenomena. In particular, depolarization of granulated sphere is determined by short-range interaction between nearby granules for very small d_g, while for d_g of order λ and larger it is determined by long-range interactions of all granules. Although, analytical expressions are not accurate enough in many cases, they can be used to construct approximate inversion techniques, which goal is to deduce information about granules from light scattering signals.

We showed that differences between experimentally measured signals of neutrophils and eosinophils [14] can be described solely by the difference in their granule sizes, which agrees with previous phenomenological descriptions of this phenomena. Moreover, calculated D_{SS} quantitatively agrees with experimental results. However, the quantitative comparison is hindered by the uncertainty of m_g. Finally, as an example of other scattering quantities we showed and discussed the dependence of extinction efficiency and asymmetry parameter on f and d_g. They can also be used to approach the inverse problem.

Acknowledgments